# INTERACTIONS OF SHEAR TRANSFORMATION BANDS

# Atomic-level study of twin-twin interactions in hexagonal metals

# Mingyu Gong<sup>1,a)</sup> Wenqian Wu<sup>1</sup>

<sup>1</sup>Department of Mechanical and Materials Engineering, University of Nebraska-Lincoln, Lincoln, Nebraska 68588, USA

Received: 16 December 2019; accepted: 4 March 2020

Twin-twin interactions (TTIs) take place when multiple twinning modes and/or twin variants are activated and interact with each other. Twin-twin junctions (TTJs) form and affect subsequent twinning/detwinning and dislocation slip, which is particularly important in determining mechanical behavior of hexagonal metals because twinning is one major deformation mode. Atomic-level study, including crystallographic analysis, transmission electronic microscopy (TEM), and molecular dynamics (MD) simulations, can provide insights into understanding the process of TTIs and structural characters associated with TTJs. Crystallographic analysis enables the classification of TTIs and the prediction of possible interfaces of twin-twin boundaries (TTBs), characters of boundary dislocations, and possible reactions of twinning dislocations and lattice dislocations at TTBs. MD simulations can explore the process of TTIs, microstructures of TTJs, atomic structures of TTBs, and stress fields associated with TTJs. The predictions based on crystallographic analysis and the findings from MD can be partially verified by TEM. More importantly, these results provide explanation for microstructural characters of TTJs and guidance for further TEM characterizations.

## Introduction

Hexagonal metals with hexagonal close-packed (HCP) structure, such as magnesium (Mg) and titanium (Ti), have wide application as structural materials. Mg and its alloys with high specific strength have potential applications in vehicle transportation and aviation to reduce weight and further to increase fuel efficiency [1, 2, 3]. Ti and its alloys are widely employed in aerospace industry and medical implants because of their high strength and good biocompatibility [4, 5, 6]. Plastic deformation is carried over by slips and twins. Basal and prismatic a slips are commonly activated [7, 8, 9, 10, 11, 12, 13] in all HCP metals, but they cannot contribute to plastic deformation along c. Nonbasal c+a dislocations on the 1st and 2nd pyramidal planes accommodate plastic deformation along c, but they have low mobility at room temperature [14, 15, 16, 17, 18]. Deformation twinning becomes an alternate deformation mode to accommodate plastic deformation along c. Six twinning modes,  $\{\bar{1}01m\}$  (m = 1, 2, 3) and  $\{11\bar{2}n\}$  (n = 1, 2, 3)2, 4) twinning, are reported for different hexagonal metals [19, 20].  $\{\overline{1012}\}$  tension twinning is easily activated [21, 22, 23, 24, 25, 26], whereas  $\{\bar{1}011\}$  and  $\{\bar{1}013\}$  compression twinning are hard to activate [27, 28, 29] in Mg at room temperature.  $\{\bar{1}012\}$  and  $\{11\bar{2}1\}$  tension twins, and  $\{11\bar{2}2\}$ ,  $\{11\bar{2}4\}$ , and  $\{\bar{1}011\}$  compression twins are observed in Ti [30, 31, 32, 33, 34, 35, 36, 37, 38, 39, 40, 41, 42].

Multiple twinning modes and their variants can be activated concurrently and interact with each other under monotonic loading [36, 43, 44, 45], cyclic loading [46, 47, 48, 49, 50], shocking [40, 51, 52], etc. Twin–twin interactions (TTIs) take place and result in the formation of twin–twin junctions (TTJs) [43, 53, 54, 55, 56, 57, 58], which cause strain hardening [49, 54, 59, 60] and crack initiation [49, 54, 59, 60]. Twin–twin boundaries (TTBs) associated with TTJs can be described as a result of reactions of twinning dislocations (TDs). Yu et al. [53] defined three types of TTBs, which are TTB<sub>I</sub> parallel to twinning planes, and TTB<sub>O</sub> and TTB<sub>A</sub> on the obtuse and acute sides of TTJs. Roberts and Partridge [61] characterized TTBs between two  $\{\bar{1}012\}$  twins. TTB<sub>O</sub> and TTB<sub>A</sub> are nearly parallel to the bisection between two twinning planes. Morrow et al. [48, 62] employed in situ transmission electronic microscopy

1647

a) Address all correspondence to this author. e-mail: mingyu@huskers.unl.edu

This paper has been selected as an Invited Feature Paper.



(TEM) to investigate twinning/detwinning behavior under cyclic loading and found that TTBs retarded detwinning process. Moreover, residual twins form in the vicinity of TTBs [49, 50], serving as sources for retwinning and inducing cyclic hardening. Local stress fields [36, 40, 63, 64] associated with TTJs affect or trigger anisotropic growth of primary twins [53, 63, 65, 66], sequential primary twinning [36, 54, 56, 57, 67], secondary twinning [40, 49, 68, 69, 70], and slip bands [71, 72]. Chen et al. [66] observed abnormal migration of twin boundaries using in situ electron backscattered diffraction (EBSD). Twin boundaries (TBs) continue to migrate when the sides of intersecting twin bands enclose an acute angle but cease to migrate on the sides enclosing an obtuse angle. The anisotropic twin growth on two sides of TTJs explains the prevalent formation of certain types of TTBs [43, 53, 63, 65]. In addition, activation of secondary twins may be related to fracture initiation because microcracks are often observed along secondary twin boundaries [49]. Therefore, the evolution of microstructures may locally deviate the orientation between two twin variants, affecting subsequent twinning/detwinning and slip behavior.

Microstructural evolution during TTIs is related to both dynamics and energetics associated with growth of twins and formation of TTBs. Crystallographic analysis offers geometric insight because twinning is unidirectional with a specific twinning plane and twinning direction. Pratt [73] analyzed the crystallography associated with {1012} TTIs in HCP metals and observed  $(10\bar{1}2)$ – $(01\bar{1}2)$  and  $(10\bar{1}2)$ – $(01\bar{1}2)$  junctions by optical microscopy. Yu et al. [53] systematically classified  $\{\bar{1}012\}$  TTIs into three types with respect to the zone axis of twinning, i.e., one cozone (with zone axes of two twins parallel to each other) and two noncozone (with zone axes of two twins nonparallel to each other) TTIs and studied crystallographic aspects of the associated TTBs, including boundary planes and boundary dislocations. Energetically favorable TTBs are predicted based on the character of boundary dislocations with the application of the Frank's law [74]. Using a similar approach, Xu et al. [43] classified interactions between two {1122} twins into three types and explained the formation of prevalent TTBs that are characterized by EBSD. At the atomic level, molecular dynamics (MD) simulations are able to explore the process of TTIs and reveal the atomic structure and energy of TTBs associated with cozone [45, 64, 71] and noncozone [63] {1012} TTIs. Highresolution transmission electronic microscopy (HRTEM) [44, 45] further reveals structural character of TTBs that were predicted using MD simulations [45, 63, 71, 75]. Besides crystallographic characteristics, local stress field associated with TTJs have been analyzed using molecular statics at the atomic level and crystal plasticity models at meso-scale [36, 40, 63, 64]. Gong et al. [63] calculated the stress fields near  $\{\bar{1}012\}$ 

noncozone TTJs via atomistic simulation and correctly predicted the associated prevalent TTBs as observed by EBSD. Kumar et al. [64] discussed the effect of stress field associated with  $\{\bar{1}012\}$  cozone TTIs on twinning using elasto-viscoplastic fast Fourier transformation (EVP-FFT). Xu et al. [40] calculated the stress field near  $(11\bar{2}2)$ – $(11\bar{2}4)$  junctions with crystal plasticity fast Fourier transform (CP-FFT) modeling and explained the formation of  $(10\bar{1}2)/(01\bar{1}2)$  secondary twins.

In this article, we present a general discussion of  $\{\bar{1}012\}$  TTIs in hexagonal metals through integrating crystallographic analysis, microscopic characterization, and MD simulation. We also slightly extend our discussion to other types of twins and illustrate the feasibility of the described strategy.

# General process and features of TTI

Figure 1 schematically shows a general process of TTI during loading and reverse loading. Figure 1(a) shows an incoming twin (notated as  $T_i$ ) approaching an encountering twin (notated as  $T_i$ ). The twin tip of  $T_i$  is described as an array of TDs. Correspondingly, a stress field is produced by the array of TDs. The stress field will affect the nucleation and motion of TDs associated with the two twins and may trigger other deformation modes. Figure 1(b) shows the formation of TTB<sub>I</sub> as  $T_i$  contacts twin boundary of  $T_i$ . TTB<sub>I</sub> represents the boundary as TDs associated with  $T_i$  pile up on the boundary of twin  $T_i$  as boundary dislocations  $b_I$ . With the thickening of  $T_i$ , more TDs are piled up on the boundary. Consequently, the local stress associated with  $T_i$  increases, which may trigger dislocation slip and/or secondary twinning in the encountering twin, as shown in Figure 1(c). Meanwhile, both twins may grow and new TTBs develop, as shown in Figure 1(d). New TTBs are referred to as TTBO and TTBA according to the angle between twinning planes of  $T_i$  and  $T_i$ . TTB<sub>O</sub> forms as the angle is obtuse, and TTBA forms as the angle is acute. They can be described as an array of boundary dislocations ( $b_{\rm O}$  or  $b_{\rm A}$ ) as a result of TDs reactions. Twin transmission is generally prohibited due to the polar nature of twinning [43, 53]. Under reverse loading, detwinning as shown in Figure 1(e) may occur. It is accomplished by either dissociation of boundary dislocations or retwinning inside primary twins. Retwinning is associated with nucleation and propagation of secondary twinning with the same twin variant as the primary twins. Besides retwinning, it is also possible that secondary twinning with the other twin variants takes place in the primary twins, as shown in Figure 1(f). Boundary dislocations may act as sources for nucleating the required TDs [53]. These reactions are determined by character of TTBs, local stress fields, and available deformation modes.

TTJs and TTBs have been characterized in Mg [44, 45, 48, 49, 50, 54, 58, 61, 62, 63, 71], Ti [36, 43, 56, 65, 72, 76], Zn [73],



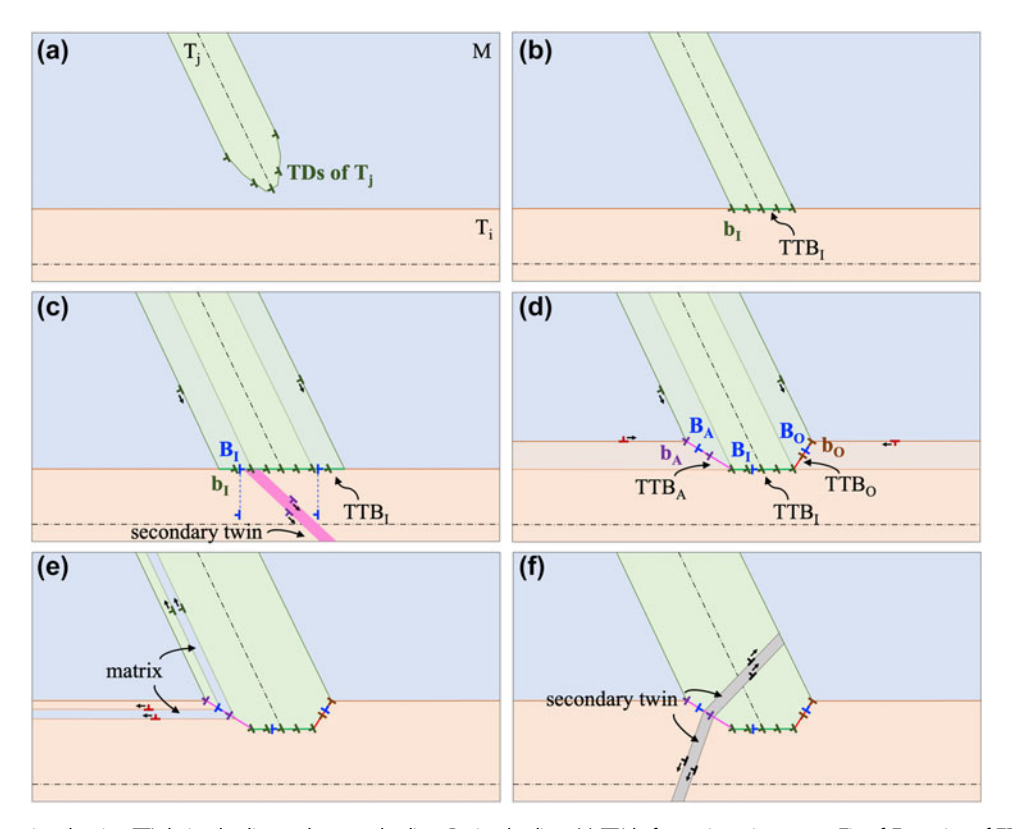


**Figure 1:** Schematics showing TTI during loading and reverse loading. During loading: (a) TTJ before twin–twin contact. Tip of  $T_j$  consists of TDs. (b) TDs of  $T_j$  reach and pile up on encountering twin  $T_i$  as  $b_i$ , forming TTB<sub>i</sub>. (c) TTB<sub>i</sub> extends while stress relaxation takes place via deformation modes (dislocation slip, secondary twinning, etc.) other than primary twinning.  $B_i$  is the misfit dislocation on TTB<sub>i</sub>. (d) TTB<sub>O</sub> and TTB<sub>A</sub> form, whereas growth of both  $T_i$  and  $T_j$  is favored on the obtuse and acute sides of TTJs. Misfit dislocations  $B_O$  and  $B_A$  form on TTB<sub>O</sub> and TTB<sub>A</sub> after stress relaxation. During reverse loading: (e) Detwinning of  $T_i$  and  $T_j$  may take place. (f) Secondary twinning in  $T_i$  and  $T_j$  may form.

Zr [55, 77, 78], and Re [67, 79] by optical microscopy [50, 61, 73], EBSD [36, 43, 49, 54, 55, 58, 63, 71, 76], and TEM [44, 45, 48, 62, 65, 67, 72, 77, 79]. To facilitate the discussion and review of these TTJs and TTBs, we followed the notation of twin variants proposed by Xu et al. [80].  $T_i^{\rm I}$  and  $T_i^{\rm II}$  ( $n=1,2,\ldots,6$ ) denote the six  $\{\bar{1}012\}$  and six  $\{11\bar{2}1\}$  twin variants, whereas  $C_i^{\rm I}$  and  $C_i^{\rm II}$  ( $n=1,2,\ldots,6$ ) represent six  $\{11\bar{2}2\}$  and six  $\{11\bar{2}4\}$  twin variants.  $T_i^{\rm I}$ ,  $T_i^{\rm II}$ ,  $C_i^{\rm I}$ , and  $C_i^{\rm II}$  represent ( $10\bar{1}2$ ), ( $11\bar{2}1$ ), ( $11\bar{2}2$ ), and ( $11\bar{2}4$ ) twin variants. The subscript changes from 1 to 6 following a counter-clockwise rotation about **c** axis. As proposed by Yu et al. [53], an interaction between incoming twin  $T_i^{\rm I}$  and encountering twin  $T_i^{\rm I}$  is denoted as  $T_i^{\rm I} \to T_i^{\rm I}$ .

Because of fast propagation of twins [81, 82, 83], the moment when twins nearly intersect is rarely captured. Figures 2(a) and 2(b) show some of the features of TTJs when incoming twins nearly reach encountering twins, as schematically shown in Figure 1(a). For  $T_4^{\rm I} \to T_1^{\rm I}$  interaction, scanning transmission electron microscope (STEM) [Figure 2(a)] characterizes a local deviation of encountering TBs from the twinning plane near the intersection point [62], indicating possible attraction of encountering TBs by incoming twins. Figure 2(b) shows several  $T_2^{\rm I} \to T_1^{\rm I}$  junctions (enclosed by

dashed circles) before they meet each other. Encountering TBs on the obtuse side of TTJs appears to be attracted by incoming twin tip, whereas the TBs on the acute side seem to be repulsed by incoming twin. Such features may be related to local stress field associated with incoming twin.

Figures 2(c)-2(f) show some typical microstructures of TTJs after the intersection of two twins. With EBSD characterization, a TTB<sub>I</sub> is observed in Mg [Figure 2(c)] associated with a  $T_3^{\rm I} \rightarrow T_1^{\rm I}$  interaction [63], a TTB<sub>O</sub> is observed in Ti [Figure 2(d)] associated with a  $C_3^{\rm I} o C_4^{\rm I}$ interaction [43], and a TTBA is observed in Mg [Figure 2(e)] associated with a  $T_4^{\rm I} \to T_1^{\rm I}$  interaction [71]. For these cases, one of the TTBs is prevalent. Figure 2(e') [71] shows a backscattered secondary electron (BSE) micrograph of the same region in Figure 2(e). A basal slip band is found connected to TTB<sub>A</sub>. Figure 2(f) shows a secondary twin  $T_5^{\rm I}$ characterized inside the primary twin  $C_1^{\text{II}}$  as  $C_4^{\text{I}} \rightarrow C_1^{\text{II}}$ interaction happens [40]. These observations can be explained schematically by Figures 1(c) and 1(d). Additionally, it should be noted that a majority of TTBs characterized by microscopy is in near-equilibrium state due to stress relaxation [84], and may not be the same as nonequilibrium TTBs upon formation [84, 85].



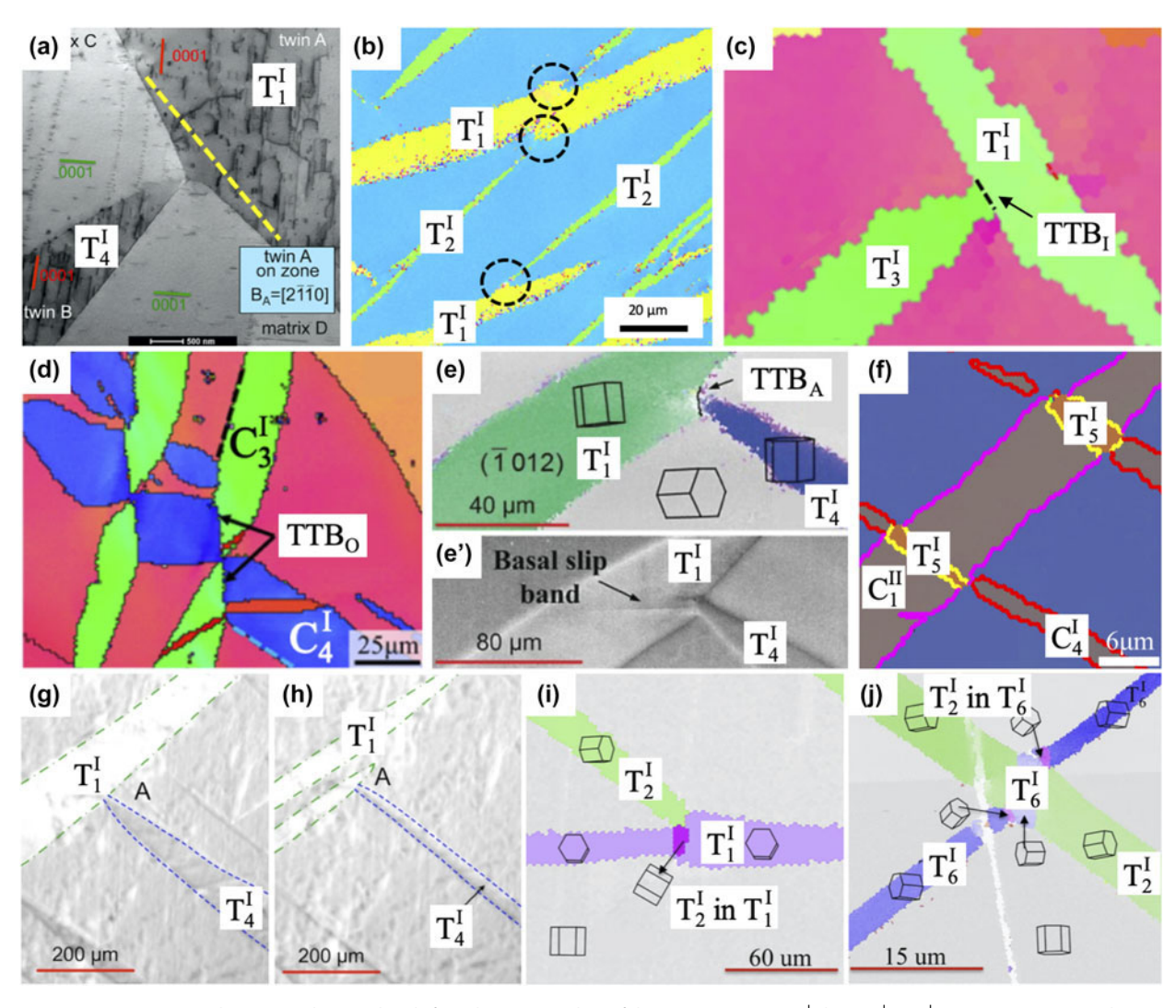


Figure 2: (a) STEM image showing TBs deviating largely from the twinning plane of the encountering twin  $T_1^l$  during  $T_4^l \to T_1^l$  interaction in Mg [62]. (b) EBSD image showing anisotropic growth of encountering twins  $T_1^l$  during  $T_2^l \to T_1^l$  interaction in Mg. EBSD images showing (c) formation of TTB<sub>1</sub> associated with  $T_3^l \to T_1^l$  interaction in Mg [63], (d) formation of TTB<sub>0</sub> associated with  $T_3^l \to T_2^l$  interaction in Ti [43], and (e) formation of TTB<sub>A</sub> associated with  $T_4^l \to T_1^l$  interaction in Mg [71]. (e') BSE micrograph showing formation of basal slip band attaching to TTBA in the same region in (e). (f) EBSD image showing secondary twin  $T_5^l$  inside primary  $T_5^l$  during  $T_5^l \to T_5^l$  interaction in Ti [40. (g) and (h) In situ optical micrographs showing detwinning associated with  $T_4^l \to T_5^l$  interaction in Mg under reverse loading [71]. EBSD images showing (i) a secondary twin  $T_2^l$  connecting to TTB inside a primary twin  $T_1^l$  for  $T_2^l \to T_1^l$  interaction, and (j) two secondary twins  $T_2^l$  connecting to TTBs inside a primary twin  $T_5^l$  interaction [53].

Under reverse loading, detwinning may happen. Yu et al. [71] observed detwinning associated with  $T_4^{\rm I} \to T_1^{\rm I}$  interaction in Mg under in situ optical microscopy. As shown in Figures 2(g) and 2(h), detwinning of  $T_1^{\rm I}$  and  $T_4^{\rm I}$  mainly takes place away from TTJs, indicating possible retardation of TTJs to detwinning. Similar observation of retardation is also characterized for  $T_2^{\rm I} \to T_1^{\rm I}$  interaction in Mg [48]. In most instances, the stress state after loading reversal also favors secondary twinning [Figure 1(h)] of the same type (tension/compression) as primary twinning. Figures 2(i) and 2(j) show the double tension twin structures in  $T_j^{\rm I} \to T_i^{\rm I}$  junctions in Mg [53, 70]. The variant selection of the secondary tension twin follows the trend that the secondary twinning plane is parallel to the intersection line between two primary twinning planes.

In other words, the  $T_j^{\text{I}}$  secondary twin forms in the  $T_i^{\text{I}}$  primary twin during  $T_i^{\text{I}} \rightarrow T_i^{\text{I}}$  interaction.

These interaction processes can be partially verified by geometry features of TTJs observed by microscopy, and could be affected by several factors such as local stress fields and available deformation modes. Further analysis can be conducted based on crystallography of TTIs and atomistic simulations.

# Crystallographic analysis of TTIs

#### Classification of TTIs

Taking  $T_j^{\rm I} \to T_i^{\rm I}$  interactions as an example, we classify them into three types,  $T_{i+1}^{\rm I} \to T_i^{\rm I}$ ,  $T_{i+2}^{\rm I} \to T_i^{\rm I}$ , and  $T_{i+3}^{\rm I} \to T_i^{\rm I}$ . For each type of TTI, positions of the twinning planes associated



with the involved twin variants are shown in Figures 3(a)-3(c)in an HCP unit cell in the matrix. The angles between twinning planes of two twins are 140°/40°, 108°/72°, and 94°/86° for  $T_{i+1}^{\text{I}} \to T_i^{\text{I}}, T_{i+2}^{\text{I}} \to T_i^{\text{I}}$ , and  $T_{i+3}^{\text{I}} \to T_i^{\text{I}}$  interactions. The zone axis of one twin variant is along the intersection between its twinning plane and the basal plane. When two twins share the same zone axis, the interaction is called cozone interaction, and the others are called noncozone interaction. Thus,  $T_{i+3}^{I} \rightarrow T_{i}^{I}$ interactions are of cozone, whereas  $T_{i+1}^{I} \to T_{i}^{I}$  and  $T_{i+2}^{I} \to T_{i}^{I}$ interactions are noncozone. For all types of TTIs, twinning planes of two twins intersect and divide a crystal into four regions. The intersection lines are along the red dashed lines  $\xi$ , which are  $[\bar{2}\bar{2}43]_M$ ,  $[0\bar{2}21]_M$ , and  $[1\bar{2}10]_M$  directions for  $T_2^{\mathrm{I}} \to T_1^{\mathrm{I}}$ ,  $T_3^{\mathrm{I}} \to T_1^{\mathrm{I}}$ , and  $T_4^{\rm I} \to T_1^{\rm I}$  interactions. The divided regions are defined as obtuse sides or acute sides depending on the angles between the two twinning planes on those sides. Two twins are bonded by TTBs: the types of which are determined by their position. TTB<sub>I</sub> is parallel to one of the twinning planes of two twins. TTBO forms on the obtuse sides, whereas TTBA forms on the acute sides. With the assumption that TTBO and TTBA are parallel to the bisection between two twinning planes, Figures 3(a')-3(c') shows positions of TTB<sub>O</sub> (blue planes) and TTB<sub>A</sub> (red planes) in an HCP unit cell in the matrix. TTB<sub>I</sub>, TTB<sub>O</sub>, and TTB<sub>A</sub> have high index in two interacting twins. Table I summarizes the index of TTBs in the matrix and two interacting twins.

Structural character associated with other TTIs can be analyzed by using a similar approach. Interactions between two twins in the same twinning mode, i.e.,  $T_j^{\rm I} \to T_i^{\rm I}$  and  $C_j^{\rm I} \to C_i^{\rm I}$ , are always classified into three types [36, 43, 53, 55, 63, 65, 76]. Interactions between two twins in different twinning modes, such as  $T_j^{\rm I} \to T_i^{\rm II}$  and  $C_j^{\rm I} \to C_i^{\rm II}$ , are classified into four types [55].

#### Formation and roles of TTBs

TTBs form as one twin encounters and reacts to another twin. TTBs form based on the reaction of TDs. When the tip of the incoming twin is blocked at the boundary of the encountering twin,  $\text{TTB}_{\text{I}}$  forms. The TTB plane coincides with the twinning plane of the encountering twin and contains boundary dislocations that have the same character as the TD associated with the incoming twin. When both twins grow through the glide of TDs, these TDs meet, react, and form junctions. The line senses of TDs are along the  $\xi$  direction upon reaction. The pileup of these boundary dislocations forms a dislocation wall, corresponding to the TTBs. Based on the angles between the two primary twinning planes, one TTB is referred to as  $\text{TTB}_{\text{A}}$  corresponding to an acute angle, and the other is referred to as  $\text{TTB}_{\text{O}}$  corresponding to an obtuse angle. The Burgers vector of the junction is thus equal to the sum of the two TDs.

A TTJ between  $T_i$  and  $T_j$  is schematically shown in Figure 4. The TTJ comprises TTB<sub>I</sub> and prevalent TTB<sub>O</sub>/TTB<sub>A</sub>.

The blue and green dashed lines represent TDs of  $T_i$  and  $T_j$ . On TTB<sub>I</sub> (green plane in Figure 4), TDs of  $T_j$  pileup on  $T_i$  as boundary dislocation b<sub>I</sub> (represented by the pink dashed line). Boundary dislocations  $b_{\rm O}$  or  $b_{\rm A}$  (represented by the brown dashed line) lie on TTB<sub>O</sub> or TTB<sub>A</sub> (orange plane in Figure 4). Line senses of b<sub>I</sub>, b<sub>O</sub>, and b<sub>A</sub> upon formation are along the  $\xi$  direction. Frank's law [74] is employed [43, 53, 63, 65] to assess the change in line energy of these dislocations  $b_{\rm I}$ ,  $b_{\rm O}$ , and  $b_{\rm A}$ . A reduction of line energy associated with the formation of boundary dislocations indicates that the reaction is energetically favorable and is likely to take place. Taking  $T_2^{\rm I} \to T_1^{\rm I}$  interaction as an example, the TDs react when their line senses are along the  $\xi$  direction ( $[\bar{2}\bar{2}43]_M$  direction). The reactions are expressed as

$$b_{
m tw}^{T_{
m I}^{
m I}} 
ightarrow b_{
m I} \quad , \qquad \qquad (1)$$

$$b_{\rm tw}^{T_{\rm l}^{\rm I}} - b_{\rm tw}^{T_{\rm 2}^{\rm I}} \to b_{\rm O} \quad , \tag{2}$$

$$b_{
m tw}^{T_{
m I}^{
m I}} + b_{
m tw}^{T_{
m 2}^{
m I}} 
ightarrow b_{
m A} \quad .$$
 (3)

Similar calculations have been applied to boundary dislocations  $b_{\rm I}$ ,  $b_{\rm O}$ , and  $b_{\rm A}$  associated with other TTIs. The Burgers vectors of boundary dislocations associated with  $T_J^{\rm I} \to T_i^{\rm I}$  and  $C_J^{\rm I} \to C_i^{\rm I}$  interactions, and values of  $|b_{\rm I}|^2/|b_{\rm tw}|^2$ ,  $|b_{\rm O}|^2/(2|b_{\rm tw}|^2)$ , and  $|b_{\rm A}|^2/(2|b_{\rm tw}|^2)$  are listed in Table II. When the values are less than unity, the corresponding reactions are energetically favorable. There is no elastic energy change after formation of TTB<sub>I</sub> because  $|b_{\rm I}|^2/|b_{\rm tw}|^2$  is one. Formation of TTB<sub>O</sub> for  $T_{\rm I}^{\rm I} \to T_{\rm I}^{\rm I}$  interaction, TTB<sub>O</sub> for  $T_{\rm I}^{\rm I} \to T_{\rm I}^{\rm I}$  interaction, TTB<sub>O</sub> for  $C_{\rm I}^{\rm I} \to C_{\rm I}^{\rm I}$  interaction, TTB<sub>A</sub> for  $C_{\rm I}^{\rm I} \to C_{\rm I}^{\rm I}$  interaction, and TTB<sub>A</sub> for  $C_{\rm I}^{\rm I} \to C_{\rm I}^{\rm I}$  interaction reduces elastic energy and are more likely.

It is noted that elastic energy changes associated with the formation of  ${\rm TTB_I}$ ,  ${\rm TTB_O}$ , and  ${\rm TTB_A}$  for  $T_3^{\rm I} \to T_1^{\rm I}$  and  $T_4^{\rm I} \to T_1^{\rm I}$  interactions are close. For these reactions, Frank's law may fail when other factors such as dislocation core energy and interface energy of TTBs are taken into account. Correspondingly, TTB<sub>I</sub> in Mg [63] for  $T_3^{\rm I} \to T_1^{\rm I}$  interaction as well as TTB<sub>O</sub> in Mg [44, 45, 71] for  $T_4^{\rm I} \to T_1^{\rm I}$  interaction, which are not predicted by Frank's law [74], are characterized experimentally. The discrepancy between experimental observation and crystallographic analysis could be ascribed to structure relaxation of interfaces, which can be investigated via atomistic simulations and stress field analysis.

As revealed in Figures 1(e) and 1(f), detwinning and secondary twinning may take place during reverse loading. Three possible modes associated with detwinning or secondary twinning are proposed by Yu et al. [53], including (i) direct detwinning via dissociation/unzipping of boundary dislocations into TDs, (ii) retwinning inside primary twins, and (iii)



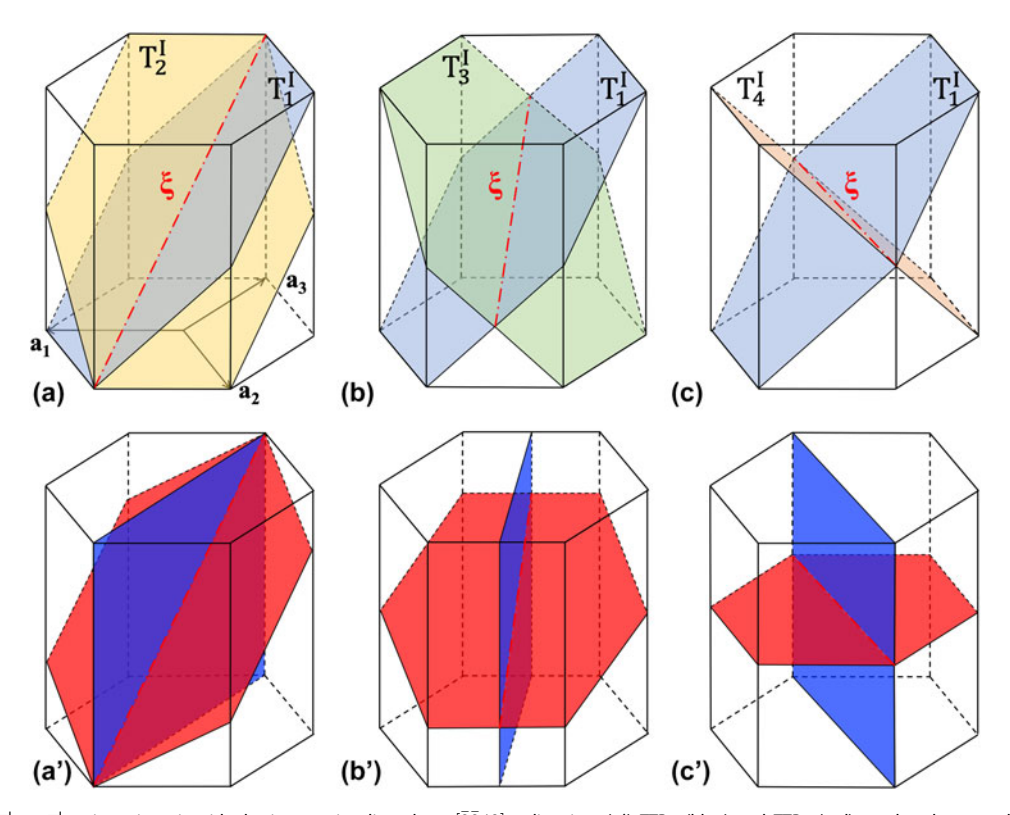


**Figure 3:** (a)  $T_2^1 \rightarrow T_1^1$  twin–twin pair with the intersection line along  $[\overline{2243}]_M$  direction. (a') TTB<sub>O</sub> (blue) and TTB<sub>A</sub> (red) on the obtuse and acute sides of  $T_2^1 \rightarrow T_1^1$  TTJ. (b)  $T_3^1 \rightarrow T_1^1$  twin–twin pair with the intersection line along  $[\overline{0221}]_M$  direction. (b') TTB<sub>O</sub> (blue) and TTB<sub>A</sub> (red) on the obtuse and acute sides of  $T_3^1 \rightarrow T_1^1$  TTJ. (c)  $T_4^1 \rightarrow T_1^1$  twin–twin pair with the intersection line along  $[\overline{1210}]_M$  direction. (c') TTB<sub>O</sub> (blue) and TTB<sub>A</sub> (red) on the obtuse and acute sides of  $T_4^1 \rightarrow T_1^1$  TTJ.

TABLE I: Index of TTBs in the matrix and two interacting twins.

		$T_2^{I} \to T_1^{I}$	$T_3^{I} \to T_1^{I}$	$T_4^{I} \to T_1^{I}$
ТТВ <sub>І</sub>	In matrix In $T_1^1$ In $T_j^1$ ( $j = 2, 3, 4$ )	$ \begin{array}{c} (10\bar{1}2)_{M} \\ (10\bar{1}2)_{T_{1}^{ }} \\ (\bar{1}\bar{5}\bar{8}23\bar{1}\bar{6})_{T_{2}^{ }} \end{array} $	$ \begin{array}{c} (10\bar{1}2)_{M} \\ (10\bar{1}2)_{T_{1}^{l}} \\ (3\bar{8}54)_{T_{2}^{l}} \end{array} $	$\begin{array}{c} (10\bar{1}2)_{M} \\ (10\bar{1}2)_{T_{1}^{l}} \\ (10\bar{1}3)_{T_{4}^{l}} \end{array}$
πвο	In matrix In $T_1^1$ In $T_j^1$ ( $j = 2, 3, 4$ )	$ \begin{array}{c} (1\ \bar{1}\ 0\ 0)_{M} \\ (9\ \bar{19}\ 10\ 18)_{T_{1}^{1}} \\ (19\ \bar{9}\ \bar{10}\ 18)_{T_{2}^{1}} \end{array} $	$\begin{array}{c} (\bar{2}110)_{M} \\ (2\bar{5}3\underline{14})_{T_{1}^{1}} \\ (23\bar{5}\overline{14})_{T_{2}^{1}} \end{array}$	$ \begin{array}{c} (10\bar{1}0)_{M}^{4} \\ (\bar{1}0129)_{T_{1}^{1}} \\ (\bar{1}01\overline{29})_{T_{2}^{1}} \end{array} $
ТТВΑ	In matrix In $T_1^1$ In $T_j^1$ ( $j = 2, 3, 4$ )	$\frac{(\frac{1}{31}\frac{1}{2}4)_{M}}{(\frac{31}{20}51\frac{62}{51})_{T_{1}^{1}}} (\frac{20}{31}51\frac{1}{62})_{T_{2}^{1}}$	$ \begin{array}{c} (01\bar{1}4)_{M} \\ (\bar{8}\bar{5}13\bar{6})_{T_{1}^{l}} \\ (8\bar{1}35\bar{6})_{T_{3}^{l}} \end{array} $	$\begin{array}{l} (0002)_{M} \\ (\bar{8}08\bar{1})_{T_{4}^{1}} \\ (80\bar{8}\bar{1})_{T_{4}^{1}} \end{array}$

secondary twinning inside primary twins. In their work, a wide range of possible reactions on  $\mathrm{TTB_I}$ ,  $\mathrm{TTB_O}$ , and  $\mathrm{TTB_A}$  are listed for  $T_j^{\mathrm{I}} \to T_i^{\mathrm{II}}$  interactions, and the associated changes in elastic energy are calculated based on Frank's law [74]. With the knowledge of prevalent TTBs, the range of possible reactions is greatly narrowed down. This also raises the necessity to investigate TTIs by atomistic simulations and stress field analysis.

#### **MD** simulations of TTIs

# Stress field analysis associated with TTIs

Atomistic simulations are able to investigate both dynamics [45, 63, 64, 71] and energetics [63, 75] associated with TTIs. As

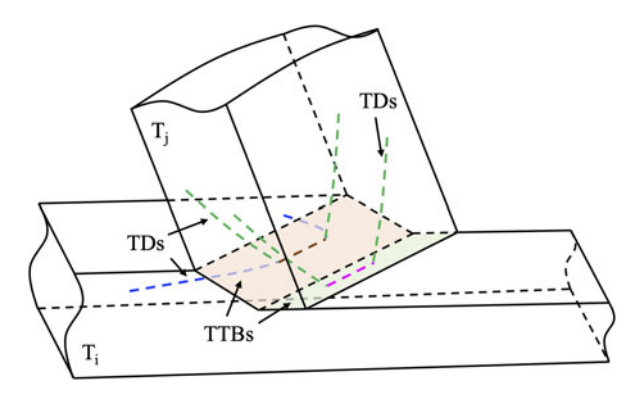


**Figure 4:** Schematics showing formation of prevalent TTB by pileup of boundary dislocations (pink and brown dashed line). The boundary dislocations form by reactions of TDs of twin i (blue dashed line) and j (green dashed line), and have line sense along the  $\xi$ .

one twin approaches another, Kumar et al. [64] numerically studied the role of local stress field on  $T_4^{\rm I} \to T_4^{\rm I}$  interactions in Mg via MD simulations and EVP-FFT models. Figure 5(a) shows the initial structure containing  $T_1^{\rm I}$  and  $T_4^{\rm I}$  twins. Atoms are colored in accordance to resolved shear stress (RSS) associated with  $T_1^{\rm I}$  twinning. Along upper and lower coherent twin boundaries (CTBs), the region near the  $T_4^{\rm I}$  twin tip shows positive RSS and is greater than the RSS in the other regions, which is confirmed by Figure 5(b), showing variation of the



**TABLE II:** Dislocations associated with the formation of TTBs for  $T_i^l \to T_i^l$  and  $C_i^l \to C_i^l$  interactions [43, 53].

Pair	bı	bo	$b_{A}$	$ b_{\rm I} ^2/ b_{\rm tw} ^2$	$ b_{\rm O} ^2/(2 b_{\rm tw} ^2)$	$ b_{\rm A} ^2/(2 b_{\rm tw} ^2)$
$T_2^{I}  o T_1^{I}$	$\lambda_1[0\bar{1}11]$	$\lambda_1[\bar{1}100]$	λ <sub>1</sub> [Ī 1 2 2]	1.00	0.27	1.74
$T_3^{\tilde{I}}  o T_1^{\hat{I}}$	$\lambda_1[1 \bar{1} 0 1]$	$\lambda_1[\bar{2}  1  1  0]$	$\lambda_1[0\bar{1}12]$	1.00	0.80	1.21
$T_4^{I}  o T_1^{I}$	$\lambda_1[10\bar{1}1]$	$2\lambda_1[\bar{1}010]$	$2\lambda_1[0\ 0\ 0\ 1]$	1.00	1.06	0.94
$C_2^{l}  o C_1^{l}$	$\lambda_2[1\bar{2}13]$	$\lambda_2[2\bar{1}\bar{1}0]$	$3\lambda_2[0\bar{1}12]$	1.00	0.14	1.86
$C_3^{\tilde{i}}  o C_1^{\tilde{i}}$	$\lambda_2[2\ \bar{1}\ \bar{1}\ 3]$	$\lambda_2[1\bar{2}16]$	$3\lambda_2[1\ 0\ \bar{1}\ 0]$	1.00	1.57	0.43
$C_4^{\dagger}  ightarrow C_1^{\dagger}$	$\lambda_2[1 \ 1 \ \bar{2} \ 3]$	$6\lambda_2[0001]$	$2\lambda_2[11\bar{2}0]$	1.00	1.43	0.57

 $<sup>^{*}\</sup>lambda_{1} = \frac{3a^{2}-c^{2}}{3a^{2}+c^{2}}; \ \lambda_{2} = \frac{2a^{2}-c^{2}}{3a^{2}+3c^{2}}.$ 

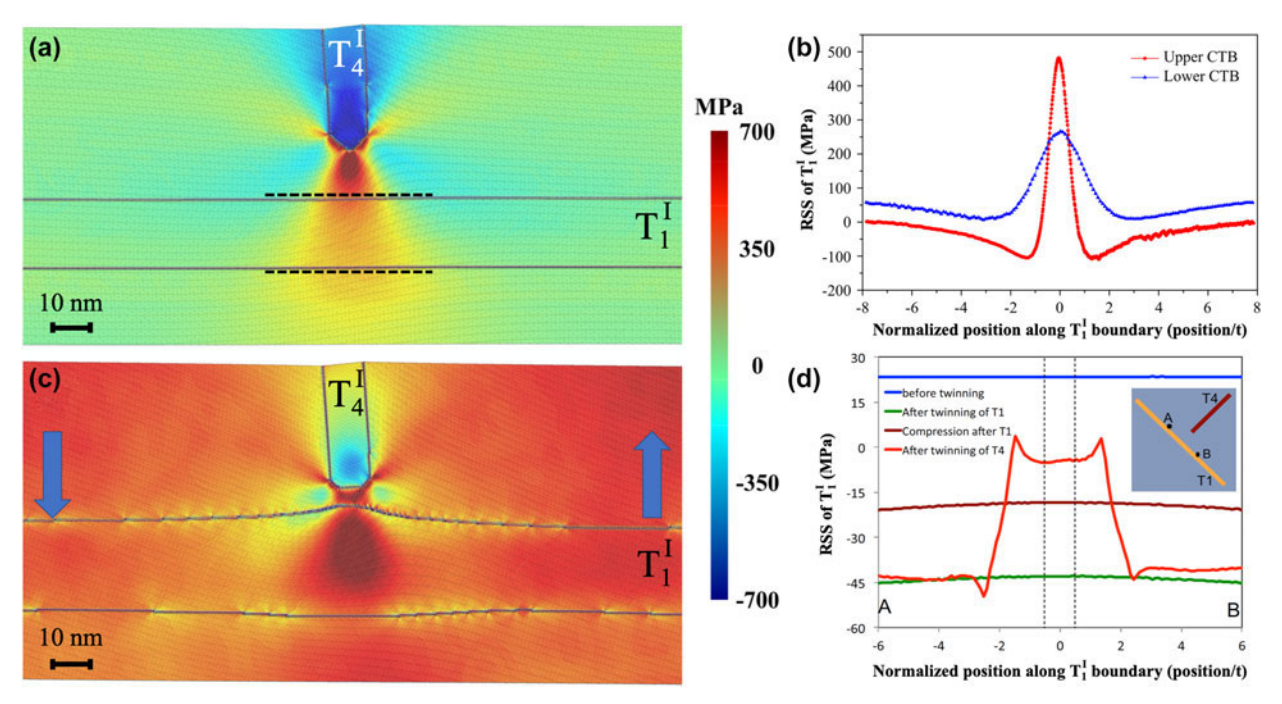


Figure 5: (a) Unloaded  $T_4^l \to T_1^l$  model for MD simulation. Atoms are colored in accordance to atomic stress (RSS of  $T_1^l$  twinning). (b) Variation of RSS associated with  $T_1^l$  twinning on upper and lower TBs along black dashed lines. (c) Under loading, upper and lower TBs of  $T_1^l$  migrate by nucleation and migration of TDs.  $T_1^l$  is in a convex shape. (d) EVP-FFT calculation of RSS associated with  $T_1^l$  twinning along top surface of  $T_1^l$  from A to B in four stages: (1) before twinning, (2) after formation of  $T_1^l$ , (3) further compression after formation of  $T_1^l$ , and (4) after formation of  $T_4^l$  [64].

RSS near upper and lower TBs along the black dashed lines. Figure 5(b) also reveals that the local RSS near the lower CTB is smaller than that near the upper CTB. Consequently, as shown in Figure 5(c), the upper CTB migrates upward and lower CTB migrates downward under a loading favoring  $T_1^{\rm I}$  twinning. The region close to the  $T_{\perp}^{I}$  twin tip migrates faster than the region far from the twin tip. The MD simulation reveals similar features to those experimentally observed [Figure 2(a)]. In comparison, Figure 5(d) shows the stress field calculated by the EVP-FFT model which displays a similar trend to that in Figure 5(b). However, the stress predicted by the EVP-FFT model is lower than that in MD simulations. This is ascribed to the lack of plastic relaxation due to the limitation of time-scale in MD simulations. The analysis of the local stress field can be applied to studies of TTIs of other types. For example, Xu et al. [36] performed continuum mechanics finite element method and correctly predicted the formation of sequential primary

twins  $T_2^{\rm I}$  or  $T_5^{\rm I}$  associated with  $T_2^{\rm II} \to T_1^{\rm II}$  interaction. Gong et al. [63] studied the local stress fields near  $T_2^{\rm I} \to T_1^{\rm I}$  and  $T_3^{\rm I} \to T_1^{\rm I}$  junctions via atomistic simulations and identified the formation of  ${\rm TTB_O}$  associated with  $T_2^{\rm I} \to T_1^{\rm I}$  interaction and  ${\rm TTB_I}$  associated with  $T_3^{\rm I} \to T_1^{\rm I}$  interaction. Xu et al. [40] performed local stress field analysis via CP-FFT modeling of  $C_3^{\rm I} \to C_6^{\rm II}$  junctions and showed the possible activation of  $T_3^{\rm I}$  or  $T_4^{\rm I}$  secondary twinning in primary twin  $C_6^{\rm II}$ .

## Formation and character of TTJs

Yu et al. [71], Sun et al. [45], and Gong et al. [63] performed MD simulations to investigate the dynamic process associated with  $T_j^{\rm I} \to T_i^{\rm I}$  interaction in Mg. Figure 6 shows MD simulations of  $T_2^{\rm I} \to T_1^{\rm I}$ ,  $T_3^{\rm I} \to T_1^{\rm I}$ , and  $T_4^{\rm I} \to T_1^{\rm I}$  interactions in Mg. Figures 6(a)–6(c) show initial structures as one twin approaches another.  $\{\bar{1}012\}$  twins are constructed according



to the shear-shuffle mechanism [84, 86, 87]. Figures 6(a')-6(c')show atomic structures of TTBs after loading for a while. A TTB<sub>I</sub> always forms when TDs of the incoming twin pileup on the encountering twin, which is schematically shown in Figure 1(b). After that, formation of TTBO associated with  $T_2^{\rm I} \to T_1^{\rm I}$  interaction, extension of TTB<sub>I</sub> associated with  $T_3^{\rm I} \rightarrow T_1^{\rm I}$  interaction, and development of both TTB<sub>O</sub> and  $TTB_A$  associated  $T_4^I \rightarrow T_1^I$  interaction are observed. These TTBs are likely to be prevalent TTBs. TTJs in MD simulations share the same features as experimentally observed [44, 45, 53, 61, 63, 77], revealing the capability of MD simulations to reproduce the interaction process. It should be noted that MD simulations can only model the evolution of TTJs with timescale limitation. The TTBs shown in Figures 6(a')-6(c') are in nonequilibrium state and are accompanied by a long-range stress field. Nonequilibrium TTBs can relax into an equilibrium state through rearrangement of dislocations on TTBs and/or emitting lattice dislocations into two twins, which can hardly be modeled by MD simulations of current models [Figures 6(a)-6(c)] because of the time-scale limitation. The atomic structures and energies of both nonequilibrium and equilibrium TTBs can be investigated by application of bicrystal models with twin-twin orientation.

#### Structures and energies of TTBs

(i) Instability of nonequilibrium TTBs. TTJs upon formation as shown in Figures 6(a')-6(c') comprise nonequilibrium TTBs associated with pileup and reaction of TDs. With the extension of nonequilibrium TTBs, increasing elastic energy is stored within the system, leading to greater possibility for TTBs to degenerate or to relax stress. MD simulations of structures shown in Figure 6 are less likely to reproduce such degeneration or stress relaxation in time-scale associated with MD because the size of TTBs as shown in Figures 6(a')-6(c') (in 2-3 nm) is much smaller than that experimentally observed, i.e., as shown in Figure 2 (in microscale). To investigate the evolution of atomic structures of nonequilibrium TTBs, we perform the MD simulations of bicrystal models containing 80-nm TTBs. The simulation model is constructed by introducing and piling up TDs associated with two twins on an imaginary TTB in a single crystal. Then, shuffling is applied to move atoms in the sheared region to twin-oriented positions. With relaxation, TDs react and boundary dislocations form. Nonequilibrium TTB<sub>O</sub> for  $T_2^{\rm I} \to T_1^{\rm I}$ interaction and TTB<sub>I</sub> for  $T_3^{\rm I} \to T_1^{\rm I}$  interaction, which are prevalent TTBs, are created following the above description. The models adopt a coordinate that ydirection is perpendicular to the imaginary TTB, z-

- direction is along intersection line  $\xi$ , and x-axis is the cross-product of y- and z-directions. Figures 7(a) and 7(b) show the nonequilibrium TTBs after relaxation at 300 K for 2 ps. Nonequilibrium TTBO associated with  $T_2^{\mathrm{I}} \to T_1^{\mathrm{I}}$  interaction is a coherent  $(1\bar{2}12)_{T_2^{\mathrm{I}}} \| (2\bar{1}\bar{1}\bar{2})_{T_2^{\mathrm{I}}} \|$ interface. The boundary dislocations bo not only compensate for the misfit between  $(1\bar{2}12)_{T_{\cdot}^{!}}$  and  $(2112)_{T^1}$  planes but also generate a long-range stress field with a large elastic energy. The nonequilibrium  $TTB_I$  associated with  $T_3^I \rightarrow T_1^I$  interaction comprises a CTB of  $T_1^{I}$  and TDs of  $T_3^{I}$ . No misfit dislocation is found, although the boundary has a long-range stress field and large elastic energy. Structures after relaxation at 300 K for 1000 ps are shown in Figures 7(a') and 7(b'). As shown in Figure 7(a'), misfit dislocations (circled by red dashed lines) form on the TTB and locally destroy the coherency of the TTB. The formation of misfit dislocation may be attributed to dislocation rearrangement and/or emission of lattice dislocations. The structure is partially relaxed due to the time-scale limitation of atomistic simulations. In Figure 7(b'), detwinning of  $T_3^{\rm I}$  is observed. The nonequilibrium prevalent TTB is stable for neither  $T_2^{\text{I}} \rightarrow T_1^{\text{I}}$  interaction nor  $T_3^{\rm I} \to T_1^{\rm I}$  interaction. The instability of the nonequilibrium TTBs should be general to all types of TTIs. In experiments, a majority of the TTBs characterized are stress-relaxed and in near-equilibrium state. Thus, there is a necessity to study atomic structures of equilibrium TTBs.
- (ii) Structures and energies of equilibrium Nonequilibrium TTBs can relax into an equilibrium state through rearrangement of dislocations on TTBs and/or emitting lattice dislocations into the two twins. It is noted that TTBs characterized in experiments are more likely to be equilibrium or nearly equilibrium TTBs. Stress relaxation may take place right after formation of TTJs, during preparation of samples and microscopy characterization. The knowledge of the structures and energies of equilibrium can help to understand the formation mechanisms and the effects on twinning/detwinning of TTBs. The atomic structures of equilibrium TTBs and corresponding interface energy can be investigated via atomistic simulations. Construction of models follows the method to construct symmetric tilt grain boundaries described by Wang et al. [88]. Relaxed structures of prevalent TTBs associated with  $T_i^{\rm I} \to T_i^{\rm I}$  interactions in Mg are shown in Figure 8. All structures adopt a coordinate that y-direction is perpendicular to the TTB, z-direction is along intersection line  $\xi$ , and x-axis is the cross-product of yand z-directions. The equilibrium TTBs comprise



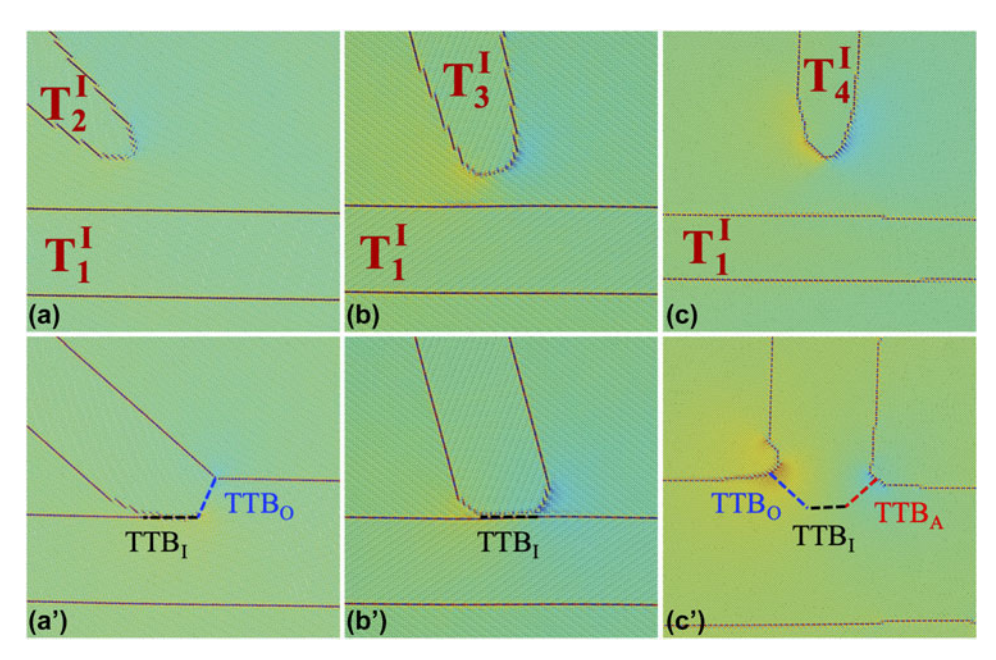


**Figure 6:** (a) Initial  $T_2^l \to T_1^l$  structure. (a') Final structure of  $T_2^l \to T_1^l$  interaction under an RSS of 500 MPa. (b) Initial  $T_3^l \to T_1^l$  structure. (b') Final structure of  $T_3^l \to T_1^l$  interaction under an RSS of 500 MPa. (c) Initial  $T_4^l \to T_1^l$  structure. (c') Final structure of  $T_4^l \to T_1^l$  interaction under an RSS of 500 MPa.

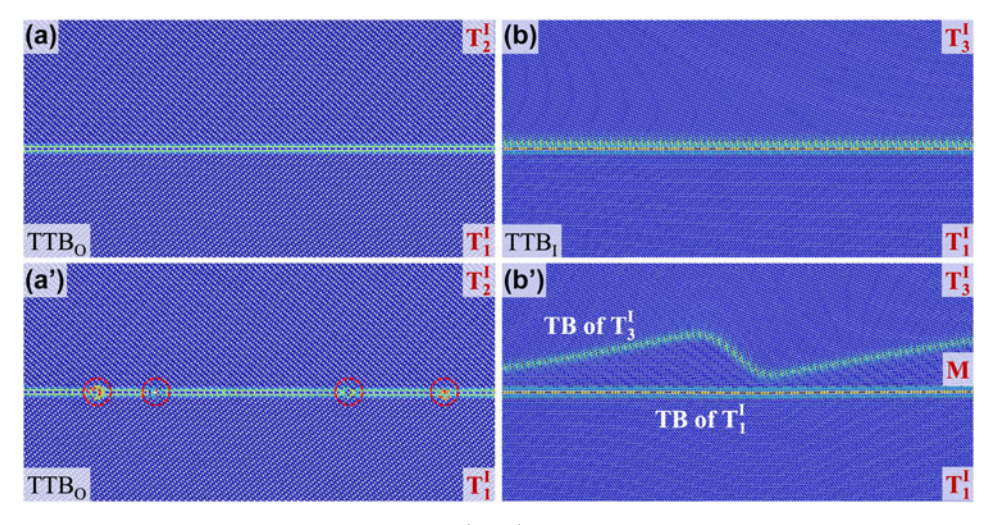


**Figure 7:** Atomic structures of the nonequilibrium TTB<sub>0</sub> associated with  $T_2^1 \rightarrow T_1^1$  interaction at 300 K for (a) 2 ps and (a') 1000 ps. Atomic structures of the nonequilibrium TTB<sub>1</sub> associated with  $T_3^1 \rightarrow T_1^1$  interaction at 300 K for (b) 2 ps and (b') 1000 ps. Atoms are colored according to excessive potential energy.

coherent TTBs and misfit dislocations. The equilibrium TTB<sub>O</sub> associated with  $T_2^{\rm I} \to T_1^{\rm I}$  interaction is shown in Figure 8(a) as semi-coherent  $(1\bar{2}12)_{T_1^{\rm I}} \| (2\bar{1}\bar{1}\bar{2})_{T_2^{\rm I}}$  interface. The Burgers vector of the misfit dislocations is equal to  $\left(0, -2d_{\{11\bar{2}2\}}\cos\frac{\phi}{2}, 0\right)$  in the current coordinate, where  $\phi=5.1^{\circ}$ . The average distance between two nearby misfit dislocations is 3.1 nm. The equilibrium TTB<sub>I</sub> associated with  $T_3^{\rm I} \to T_1^{\rm I}$  interaction is shown in Figure 8(b) and is parallel to  $(10\bar{1}2)_{T_1^{\rm I}}$  planes. The misfit dislocation is equal to  $\beta[1\bar{1}01]_{T_3^{\rm I}}$ , where  $\beta=-0.47$ . The average distance between two nearby misfit

dislocations is 3.0 nm, which is around 15 times the  $\{10\bar{1}2\}$  interplanar distance. Figures 8(c) and 8(d) show the equilibrium  $\text{TTB}_{\text{O}}$  and  $\text{TTB}_{\text{A}}$  associated with  $T_4^{\text{I}} \to T_1^{\text{I}}$  interaction. The structures are single crystals with misfit dislocations. For the  $\text{TTB}_{\text{O}}$ , the Burgers vector of the misfit dislocations is equal to  $(\pm d_{\{0002\}}\sin\frac{\varphi}{2},d_{\{0002\}}\cos\frac{\varphi}{2},0) \text{ in the current coordinate, where } \varphi=7.2^{\circ}.$  The average distance between two nearby misfit dislocations is 1.9 nm. For the  $\text{TTB}_{\text{A}}$ , the misfit dislocations are a dislocations with opposite screw components. The average distance



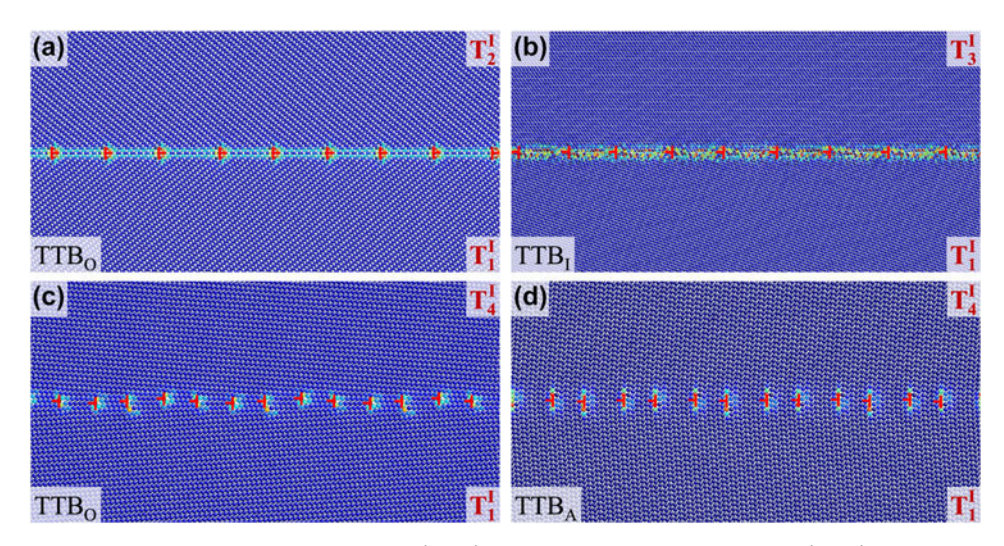


Figure 8: Atomic structures of equilibrium (a) TTB<sub>O</sub> associated with  $T_2^l \to T_1^l$  interaction [63], (b) TTB<sub>I</sub> associated with  $T_3^l \to T_1^l$  interaction, (c) TTB<sub>O</sub>, and (d) TTB<sub>A</sub> associated with  $T_4^l \to T_1^l$  interaction. Atoms are colored according to excessive potential energy.

between two nearby misfit dislocations is 2.3 nm. Similar approach can be applied to obtain atomic structures of prevalent TTBs for other TTIs. We further relax equilibrium TTB<sub>I</sub>, TTB<sub>O</sub>, and TTB<sub>A</sub> for  $T_i^{\rm I} \to T_i^{\rm I}$ interactions in Mg and  $C_i^{\mathrm{I}} \to C_i^{\mathrm{I}}$  interactions in Ti. The associated interface energies are calculated and listed in Table III. The TTB<sub>O</sub> associated with  $T_2^{\rm I} \rightarrow T_1^{\rm I}$ interaction, the  $TTB_A$  associated with  $T_3^I \rightarrow T_1^I$ interaction, the TTB<sub>A</sub> associated with  $T_4^{\rm I} \rightarrow T_1^{\rm I}$ interaction, the TTB<sub>A</sub> associated with  $C_2^{\rm I} \rightarrow C_1^{\rm I}$ interaction, the TTB<sub>O</sub> associated with  $C_3^{\rm I} \rightarrow C_1^{\rm I}$ interaction, and the TTB<sub>O</sub> associated with  $C_4^{\rm I} \to C_1^{\rm I}$ interaction have the lowest interface energy. However, in experiments [43, 44, 45, 63, 71], only TTBO for  $T_2^{\rm I} \rightarrow T_1^{\rm I}$ interaction and TTB<sub>A</sub> for  $T_4^{\text{I}} \rightarrow T_1^{\text{I}}$  interaction are prevalent TTBs. The other TTBs with the lowest interface energies are rarely observed. Formation of prevalent TTBs with large interface energy depends on the stress relaxation during interactions. The dynamic process must precede the energetics process [63].

# **Conclusions**

We present a general discussion of TTIs in hexagonal metals through integrating crystallographic analysis, microscopic characterization, MD simulation, and stress field analysis. Features of microstructures, such as anisotropic primary twin growth, formation of prevalent TTBs, slip bands, and secondary twinning can be predicted by the application of crystallographic analysis, MD simulations, and/or stress field analysis. The application of Frank's law in crystallographic analysis can

**TABLE III:** Interface energies of TTBs associated with  $T_j^l \to T_i^l$  and  $C_j^l \to C_i^l$  interactions.

	Interface energy (mJ/m²)		
Pair	TTB <sub>I</sub>	TTB <sub>O</sub>	TTB <sub>A</sub>
$T_2 \rightarrow T_1 I$	342	242	352
$T_3^{I} \to T_1^{I}$	342	363	282
$T_3^{l}  ightarrow T_1^{l} \ T_4^{l}  ightarrow T_1^{l}$	242	208	190
$C_2^{l}  o \hat{C_1^{l}}$	716	900	550
$C_2^{I}  ightarrow C_1^{I} \ C_3^{I}  ightarrow C_1^{I}$	910	860	950
$C_4^{\vec{i}}  o C_1^{\vec{i}}$	913	700	860

partially predict prevalent TTBs observed in experiments, but may fail in some circumstances. In these circumstances, changes in elastic energy associated with the formation of TTB<sub>I</sub>, TTB<sub>O</sub>, and TTB<sub>A</sub> are close. So, kinetics and energies other than elastic energy should be considered during the investigation. Stress field analysis associated with TTJs provide insights into understanding the failure of crystallographic analysis. MD simulations reveal the process of TTIs, i.e., formation of TTJs, and characterize atomic structures of equilibrium and nonequilibrium TTBs. Equilibrium TTBs with low interface energies may not be prevalent TTBs, implying the importance of dynamics associated with TTIs, because nonequilibrium TTBs with high interface energy can be relaxed into equilibrium or nearly equilibrium TTBs through rearrangement of boundary dislocations and/or nucleation and emission of lattice dislocations.

# **Acknowledgments**

This work was fully funded by the US National Science Foundation (NSF) (CMMI-1661686). Atomistic simulations



were completed utilizing the Holland Computing Center of the University of Nebraska, which receives support from the Nebraska Research Initiative.

#### References

- 1. E. Aghion and B. Bronfin: Magnesium alloys development towards the 21st century. *Mater. Sci. Forum* 350–351, **19** (2000).
- I. Polmear: Magnesium alloys and applications. *Mater. Sci. Technol.* 10, 1 (1994).
- 3. S.N. Mathaudhu and E.A. Nyberg: Magnesium alloys in US military applications: Past, current, and future solutions. In Essential Readings in Magnesium Technology, edited by S.N. Mathaudhu, A.A. Luo, N.R. Neelameggham, E.A. Nyberg, and W.H. Sillekens (Springer, Cham, Switzerland, 2016), p. 71.
- A. Astarita, C. Testani, F. Scherillo, A. Squillace, and L. Carrino:
   Beta forging of a Ti6Al4V component for aeronautic applications:
   Microstructure evolution. *Metallogr., Microstruct., Anal.* 3, 460
   (2014).
- F. Froes: Titanium: Physical Metallurgy, Processing, and Applications (ASM International, Materials Park, Ohio, 2015).
- **6. C. Leyens and M. Peters**: *Titanium and Titanium Alloys*: *Fundamentals and Applications* (Wiley-VCH, Weinheim, Germany, 2003).
- E. Schmid: Contribution to the physics and metallography of magnesium. Z. Electrochem. 37, 447 (1931).
- 8. P.W. Bakarian: Glide and Twinning in Magnesium Single Crystals at Elevated Temperatures (Yale University, New Haven, Connecticut, 1941).
- H. Conrad and W. Robertson: Effect of temperature on the flow stress and strain-hardening coefficient of magnesium single crystals. *JOM* 9, 503 (1957).
- A. Akhtar and E. Teghtsoonian: Solid solution strengthening of magnesium single crystals—I alloying behaviour in basal slip. *Acta Metall.* 17, 1339 (1969).
- A. Akhtar and E. Teghtsoonian: Substitutional solution hardening of magnesium single crystals. *Philos. Mag.* 25, 897 (1972).
- 12. L. Wang, Z. Zheng, H. Phukan, P. Kenesei, J.S. Park, J. Lind, R.M. Suter, and T.R. Bieler: Direct measurement of critical resolved shear stress of prismatic and basal slip in polycrystalline Ti using high energy X-ray diffraction microscopy. *Acta Mater*. 132, 598 (2017).
- B. Barkia, V. Doquet, J.P. Couzinié, I. Guillot, and
   E. Héripré: In situ monitoring of the deformation mechanisms in titanium with different oxygen contents. *Mater. Sci. Eng.*, A 636, 91 (2015).
- 14. P.W. Flynn, J. Mote, and J.E. Dorn: On the thermally activated mechanism of prismatic slip in magnesium single crystals. *Trans. Metall. Soc. AIME* 221, 1148 (1961).
- **15. K.Y. Xie, Z. Alam, A. Caffee, and K.J. Hemker**: Pyramidal I slip in *c*-axis compressed Mg single crystals. *Scr. Mater.* **112**, 75 (2016).

- Z. Wu, M.F. Francis, and W.A. Curtin: Magnesium interatomic potential for simulating plasticity and fracture phenomena. *Modell. Simul. Mater. Sci. Eng.* 23, 045004 (2015).
- J. Williams, R. Baggerly, and N. Paton: Deformation behavior of HCP Ti–Al alloy single crystals. *Metall. Mater. Trans. A* 33, 837 (2002).
- 18. J. Gong and A.J. Wilkinson: Anisotropy in the plastic flow properties of single-crystal α titanium determined from microcantilever beams. *Acta Mater.* 57, 5693 (2009).
- **19. J.W. Christian and S. Mahajan**: Deformation twinning. *Prog. Mater. Sci.* **39**, 1 (1995).
- G.C. Kaschner, C.N. Tomé, R.J. McCabe, A. Misra, S.C. Vogel, and D.W. Brown: Exploring the dislocation/twin interactions in zirconium. *Mater. Sci. Eng.*, A 463, 122 (2007).
- **21. A. Chapuis and J.H. Driver**: Temperature dependency of slip and twinning in plane strain compressed magnesium single crystals. *Acta Mater.* **59**, 1986 (2011).
- **22. H. El Kadiri, C.D. Barrett, J. Wang, and C.N. Tomé**: Why are  $\{10\overline{1}2\}$  twins profuse in magnesium? *Acta Mater.* **85**, 354 (2015).
- A. Serra, D.J. Bacon, and R.C. Pond: Dislocations in interfaces in the hcp metals—I. Defects formed by absorption of crystal dislocations. *Acta Mater.* 47, 1425 (1999).
- 24. Z. Zhang, H. Sheng, Z. Wang, B. Gludovatz, Z. Zhang, E.P. George, Q. Yu, S.X. Mao, and R.O. Ritchie: Dislocation mechanisms and 3D twin architectures generate exceptional strength-ductility-toughness combination in CrCoNi mediumentropy alloy. Nat. Commun. 8, 14390 (2017).
- 25. B-Y. Liu, J. Wang, B. Li, L. Lu, X.Y. Zhang, Z-W. Shan, J. Li, C-L. Jia, J. Shu, and E. Ma: Twinning-like lattice reorientation without a crystallographic twinning plane. *Nat. Commun.* 5, 1 (2014).
- I. Beyerlein, L. Capolungo, P. Marshall, R. McCabe, and
   C. Tomé: Statistical analyses of deformation twinning in magnesium. *Philos. Mag.* 90, 2161 (2010).
- **27. R.E. Reed-Hill**: A study of the (1011) and (1013) twinning modes in magnesium. *Trans. Am. Inst. Min. Metall. Eng.* **218**, 554 (1960).
- 28. H. Yoshinaga and R. Horiuchi: Deformation mechanisms in magnesium single crystals compressed in the direction parallel to hexagonal axis. *Trans. Jpn. Inst. Met.* 4, 1 (1963).
- **29. H. Yoshinaga, T. Obara, and S. Morozumi**: Twinning deformation in magnesium compressed along the *C*-axis. *Mater. Sci. Eng.* **12,** 255 (1973).
- **30.** T. Bieler, P. Eisenlohr, C. Zhang, H. Phukan, and M. Crimp: Grain boundaries and interfaces in slip transfer. *Curr. Opin. Solid State Mater. Sci.* **18**, 212 (2014).
- A.A. Salem, S.R. Kalidindi, and R.D. Doherty: Strain hardening of titanium: Role of deformation twinning. *Acta Mater.* 51, 4225 (2003).
- **32. S. Mullins and B.M. Patchett**: Deformation microstructures in titanium sheet metal. *Metall. Trans. A* **12**, 853 (1981).



- L. Capolungo and I. Beyerlein: Nucleation and stability of twins in hcp metals. *Phys. Rev. B* 78, 024117 (2008).
- 34. S. Jin, K. Marthinsen, and Y. Li: Formation of {1121} twin boundaries in titanium by kinking mechanism through accumulative dislocation slip. *Acta Mater.* 120, 403 (2016).
- 35. L. Wang, R. Barabash, T. Bieler, W. Liu, and P. Eisenlohr: Study of  $\{11\overline{2}1\}$  twinning in  $\alpha$ -Ti by EBSD and Laue microdiffraction. *Metall. Mater. Trans. A* **44**, 3664 (2013).
- **36.** S. Xu, M. Gong, C. Schuman, J-S. Lecomte, X. Xie, and J. Wang: Sequential  $\{10\overline{1}2\}$  twinning stimulated by other twins in titanium. *Acta Mater.* **132**, 57 (2017).
- S. Wang, Y. Zhang, C. Schuman, J-S. Lecomte, X. Zhao, L. Zuo, M-J. Philippe, and C. Esling: Study of twinning/detwinning behaviors of Ti by interrupted in situ tensile tests. *Acta Mater.* 82, 424 (2015).
- S.J. Lainé and K.M. Knowles: {1124} deformation twinning in commercial purity titanium at room temperature. *Philos. Mag.* 95, 2153 (2015).
- F. Xu, X. Zhang, H. Ni, and Q. Liu: {1124} deformation twinning in pure Ti during dynamic plastic deformation. *Mater. Sci. Eng., A* 541, 190 (2012).
- **40. S. Xu, P. Zhou, G. Liu, D. Xiao, M. Gong, and J. Wang**: Shockinduced two types of  $\{10\overline{1}2\}$  sequential twinning in titanium. *Acta Mater.* **165**, 547 (2019).
- **41.** Y.J. Li, Y.L. Chen, J.C. Walmsley, R.H. Mathinsen, S. Dumoulin, and H.J. Roven: Faceted interfacial structure of {1011} twins in Ti formed during equal channel angular pressing. *Scr. Mater.* **62**, 443–446 (2010).
- **42. Z. Zeng, S. Jonsson, and H.J. Roven**: The effects of deformation conditions on microstructure and texture of commercially pure Ti. *Acta Mater.* **57**, 5822 (2009).
- 43. S. Xu, M. Gong, X. Xie, Y. Liu, C. Schuman, J-S. Lecomte, and J. Wang: Crystallographic characters of {1122} twin-twin junctions in titanium. *Philos. Mag. Lett.* 97, 429–441 (2017).
- **44. Q. Sun, X.Y. Zhang, Y. Ren, L. Tan, and J. Tu**: Observations on the intersection between {1012} twin variants sharing the same zone axis in deformed magnesium alloy. *Mater. Charact.* **109**, 160 (2015).
- Q. Sun, A. Ostapovets, X. Zhang, L. Tan, and Q. Liu: Investigation of twin-twin interaction in deformed magnesium alloy. *Philos. Mag.* 98, 741 (2018).
- 46. S. Sinha and N. Gurao: In situ electron backscatter diffraction study of twinning in commercially pure titanium during tensioncompression deformation and annealing. *Mater. Des.* 116, 686 (2017).
- **47. L. Xiao and Y. Umakoshi**: Orientation dependence of cyclic deformation behavior and dislocation structure in Ti–5 at.% Al single crystals. *Mater. Sci. Eng.*, A **339**, 63 (2003).
- **48.** B.M. Morrow, R.J. McCabe, E.K. Cerreta, and C.N. Tomé: In situ TEM observation of twinning and detwinning during cyclic loading in Mg. *Metall. Mater. Trans. A* **45**, 36 (2014).

- 49. Q. Yu, Y. Jiang, and J. Wang: Cyclic deformation and fatigue damage in single-crystal magnesium under fully reversed straincontrolled tension–compression in the [1010] direction. Scr. Mater. 96, 41 (2015).
- 50. Q. Yu, J. Zhang, and Y. Jiang: Direct observation of twinning–detwinning–retwinning on magnesium single crystal subjected to strain-controlled cyclic tension–compression in [0 0 0 1] direction. *Philos. Mag. Lett.* 91, 757 (2011).
- 51. P. Zhou, S. Xu, D. Xiao, C. Jiang, Y. Hu, and J. Wang: Shock-induced  $\{11\overline{2}1\} \rightarrow \{11\overline{2}2\}$  double twinning in titanium. *Int. J. Plast.* 112, 194 (2019).
- **52. D. Chichili, K. Ramesh, and K. Hemker**: The high-strain-rate response of alpha-titanium: Experiments, deformation mechanisms, and modeling. *Acta Mater.* **46**, 1025 (1998).
- 53. Q. Yu, J. Wang, Y. Jiang, R.J. McCabe, N. Li, and C.N. Tomé: Twin-twin interactions in magnesium. *Acta Mater.* 77, 28 (2014).
- 54. H. El Kadiri, J. Kapil, A.L. Oppedal, L.G. Hector, S.R. Agnew, M. Cherkaoui, and S.C. Vogel: The effect of twin-twin interactions on the nucleation and propagation of twinning in magnesium. *Acta Mater.* 61, 3549 (2013).
- 55. P.A. Juan, C. Pradalier, S. Berbenni, R.J. McCabe, C.N. Tomé, and L. Capolungo: A statistical analysis of the influence of microstructure and twin-twin junctions on twin nucleation and twin growth in Zr. Acta Mater. 95, 399 (2015).
- 56. F. Rosi: Twin intersections in titanium. Acta Metall. 5, 337–339 (1957).
- 57. S-G. Hong, S.H. Park, and C.S. Lee: Strain path dependence of  $\{10\bar{1}2\}$  twinning activity in a polycrystalline magnesium alloy. *Scr. Mater.* **64**, 145 (2011).
- **58. D. Shi, T. Liu, D. Hou, H. Chen, F. Pan, and H. Chen**: The effect of twin–twin interaction in Mg–3Al–1Zn alloy during compression. *J. Alloys Compd.* **685**, 428 (2016).
- 59. L. Jiang, J.J. Jonas, A.A. Luo, A.K. Sachdev, and S. Godet: Influence of {1012} extension twinning on the flow behavior of AZ31 Mg alloy. *Mater. Sci. Eng., A* 445, 302 (2007).
- 60. G-D. Sim, G. Kim, S. Lavenstein, M.H. Hamza, H. Fan, and J.A. El-Awady: Anomalous hardening in magnesium driven by a size-dependent transition in deformation modes. *Acta Mater*. 144, 11 (2018).
- **61. E. Roberts and P.G. Partridge**: The accommodation around {1012} (1011) twins in magnesium. *Acta Metall.* **14**, 513 (1966).
- 62. B.M. Morrow, E.K. Cerreta, R.J. McCabe, and C.N. Tome: Toward understanding twin–twin interactions in hcp metals: Utilizing multiscale techniques to characterize deformation mechanisms in magnesium. *Mater. Sci. Eng.*, A 613, 365 (2014).
- **63. M. Gong, S. Xu, Y. Jiang, Y. Liu, and J. Wang**: Structural characteristics of  $\{1\bar{0}12\}$  non-cozone twin-twin interactions in magnesium. *Acta Mater.* **159**, 65 (2018).
- **64.** M.A. Kumar, M. Gong, I. Beyerlein, J. Wang, and C.N. Tomé: Role of local stresses on co-zone twin-twin junction formation in HCP magnesium. *Acta Mater.* **168**, 353 (2019).



- 65. X. Li, J. Li, B. Zhou, M. Yu, and M. Sui: Interaction of  $\{11\overline{2}2\}$ twin variants in hexagonal close-packed titanium. J. Mater. Sci. Technol. 35, 660 (2019).
- 66. H. Chen, T. Liu, S. Xiang, and Y. Liang: Abnormal migration of twin boundaries in rolled AZ31 alloy containing intersecting  $\{1\bar{0}12\}$  extension twins. J. Alloys Compd. **690**, 376 (2017).
- 67. J.E. Sabisch and A.M. Minor: Microstructural evolution of rhenium part I: Compression. Mater. Sci. Eng., A 732, 251 (2018).
- **68.** P. Chen, F. Wang, J. Ombogo, and B. Li: Formation of  $60^{\circ} \langle 01\overline{1}0 \rangle$ boundaries between  $\{10\overline{1}2\}$  twin variants in deformation of a magnesium alloy. Mater. Sci. Eng., A 739, 173 (2019).
- 69. Z-Z. Shi, J-Y. Xu, J. Yu, and X-F. Liu: Intragranular cross-level twin pairs in AZ31 Mg alloy after sequential biaxial compressions. J. Alloys Compd. 749, 52 (2018).
- 70. A. Jäger, A. Ostapovets, P. Molnár, and P. Lejček:  $\{10\overline{1}2\}-\{10\overline{1}2\}$  double twinning in magnesium. Philos. Mag. Lett. 91, 537 (2011).
- 71. Q. Yu, J. Wang, Y. Jiang, R.J. McCabe, and C.N. Tomé: Co-zone  $\{\bar{1}012\}$  twin interaction in magnesium single crystal. Mater. Res. Lett. 2, 82 (2014).
- 72. H. Li, X. Xu, Q. Sun, X. Zhang, X. Fang, and M. Zhu: Investigation of interfacial feature and interactional behavior of {1122} twin in deformed titanium. J. Alloys Compd. 788, 1137 (2019).
- 73. P.L. Pratt and S.F. Pugh: The movement of twins, kinks, and mosaic walls in zinc. Acta Metall. 1, 218 (1953).
- 74. J.P. Hirth and J. Lothe: Theory of Dislocations, 2nd ed. (Wiley, New York, 1982).
- 75. A. Ostapovets, J. Buršík, K. Krahula, L. Král, and A. Serra: On the relationship between and conjugate twins and double extension twins in rolled pure Mg. Philos. Mag. 97, 1088 (2017).
- 76. Z. Huang, P. Yong, N. Liang, and Y. Li: Slip, twinning and twintwin interaction in a gradient structured titanium. Mater. Charact. 149, 52 (2019).
- 77. B.M. Morrow, R.J. McCabe, E.K. Cerreta, and C.N. Tomé: Observations of the atomic structure of tensile and compressive

- twin boundaries and twin-twin interactions in zirconium. Metall. Mater. Trans. A 45, 5891 (2014).
- 78. R. Reed-Hill and E. Buchanan: Zig-zag twins in zirconium. Acta Metall. 11, 73-75 (1963).
- 79. J.E. Sabisch and A.M. Minor: Microstructural evolution of rhenium part II: Tension. Mater. Sci. Eng., A 732, 259 (2018).
- 80. S. Xu, M. Gong, Y. Jiang, C. Schuman, J-S. Lecomte, and J. Wang: Secondary twin variant selection in four types of double twins in titanium. Acta Mater. 152, 58 (2018).
- 81. H. Wang, P.D. Wu, J. Wang, and C.N. Tomé: A crystal plasticity model for hexagonal close packed (HCP) crystals including twinning and de-twinning mechanisms. Int. J. Plast. 49, 36 (2013).
- 82. Y. Liu, P. Tang, M. Gong, R. McCabe, J. Wang, and C. Tomé: Three-dimensional character of the deformation twin in magnesium. Nat. Commun. 10, 3308 (2019).
- 83. M. Gong, G. Liu, J. Wang, L. Capolungo, and C.N. Tomé: Atomistic simulations of interaction between basal  $\langle a \rangle$  dislocations and three-dimensional twins in magnesium. Acta Mater. 155, 187 (2018).
- 84. M. Gong, J.P. Hirth, Y. Liu, Y. Shen, and J. Wang: Interface structures and twinning mechanisms of twins in hexagonal metals. Mater. Res. Lett. 5, 449-464 (2017).
- 85. J.P. Hirth, J. Wang, and C.N. Tomé: Disconnections and other defects associated with twin interfaces. Prog. Mater. Sci. 83, 417
- 86. J. Wang, J.P. Hirth, and C.N. Tomé: (1012) twinning nucleation mechanisms in hexagonal-close-packed crystals. Acta Mater. 57, 5521 (2009).
- 87. R.C. Pond, A. Serra, and A.P. Sutton: The crystallography and atomic structure of line defects in twin boundaries in hexagonalclose-packed metals. Metall. Mater. Trans. A 22, 1185 (1991).
- **88.** J. Wang and I.J. Beyerlein: Atomic structures of  $[0\overline{1}10]$  symmetric tilt grain boundaries in hexagonal close-packed (hcp) crystals. Metall. Mater. Trans. A 43, 3556 (2012).